Anomalies in the switching dynamics of *C*-type antiferromagnets and antiferromagnetic nanowires

H. Y. Yuan,[1] Man-Hong Yung,[2,*] and X. R. Wang[3,4,†]

[1]*Department of Physics, Southern University of Science and Technology, Shenzhen 518055, Guangdong, China*

[2]*Institute for Quantum Science and Engineering and Department of Physics, Southern University of Science and Technology, Shenzhen 518055, Guangdong, China*

[3]*Department of Physics, Hong Kong University of Science and Technology, Clear Water Bay, Kowloon, Hong Kong*

[4]*HKUST Shenzhen Research Institute, Shenzhen 518057, Guangdong, China*

(Received 6 August 2019; revised manuscript received 4 September 2019; published 28 October 2019)

Antiferromagnets (AFMs) are widely believed to be superior to ferromagnets in spintronics because of their high stability due to the vanishingly small stray field. It is thus expected that the order parameter of AFMs should always align along the easy axis of the crystalline anisotropy. In contrast to this conventional wisdom, we find that the AFM order parameter switches away from the easy axis below a critical anisotropy strength when an AFM is properly tailored into a nanostructure. The switching time first decreases and then increases with the damping. Above the critical anisotropy, the AFM order parameter is stable and precesses under a microwave excitation. However, the absorption peak is not at resonance frequency even for magnetic damping as low as 0.01. To resolve these anomalies, we first ascertain the hidden role of dipolar interaction that reconstructs the energy landscape of the nanosystem and propose a model of a damped nonlinear pendulum to explain the switching behavior. In this framework, the second anomaly appears when an AFM is close to the boundary between underdamped and overdamped phases, where the observed absorption line shape has a small quality factor and thus is not reliable any longer. Our results should be significant to extract the magnetic parameters through resonance techniques.

DOI: 10.1103/PhysRevResearch.1.033052

I. INTRODUCTION

Ferromagnets played a vital role in the early development of magnetism, as well as modern spintronics, while studies and applications of antiferromagnets (AFMs) are quite limited due to their lack of tunability and are thus useless. In the past few years, AFMs have started to attract significant attention after the discovery of an electrical knob to control antiferromagnetic order in a class of antiferromagnets with broken inversion symmetry [1,2]. Various aspects, such as a damping mechanism [3,4], spin transfer torque [5–8], magnetic switching [1], spin pumping [9], and domain-wall/skyrmion dynamics [10–19], have been extensively investigated. One strong motivation of such intense interest in AFMs is their abundance in nature and intriguing stability due to the vanishingly small magnetostatic interaction (MI), which is ever doomed to be its drawback. Accordingly, MI is neglected in most of the theoretical and numerical studies of AFMs [10–13]. Nevertheless, the magnetic dipoles are there and the distribution of the dipoles in an AFM will potentially influence the magnetic energy and thus the magnetization dynamics, similar to the situation of electric dipoles in dielectric materials such as liquid crystals [20]. One open question is when and how the MIs manifest themselves and influence the magnetization dynamics. A complete understanding of this issue may help us in designing AFM-based devices that are truly free from the perturbation of magnetic charges.

In this work we take a step toward showing that MI can induce a switching of an AFM order when its crystalline anisotropy is below a critical value. The switching occurs at an ultrafast scale and widely exists in *C*-type AFMs and AFM nanowires. By analytically calculating the interaction of magnetic charges, we find that MI produces an effective anisotropy that is quadratic in magnetic order and thus reconstructs the energy landscape of the system, which has an observable effect on magnetization switching and the spin-wave spectrum. Above the critical anisotropy, an AFM resonance is observed, but the absorption peak is not positioned at the true resonance frequency when the magnetic damping is close to a critical value around 0.01. A detailed analysis shows that the quality factor of the absorption line shape is significantly reduced by the critical damping, near which the system enters the overdamped regime and the Kittel theory based on the Lorentz line shape fails.

This article is organized as follows. Our model, methodologies, and main findings are presented in Sec. II. In Sec. III we explain the anomalous resonance behavior near the phase boundaries and list the typical order of critical damping for the commonly used AFMs. A discussion and summary are given in Sec. IV.

II. MODEL AND RESULTS

We first consider a two-sublattice antiferromagnetic nanowire with an easy axis along the longitudinal direction

*yung@sustech.edu.cn
†phxwan@ust.hk

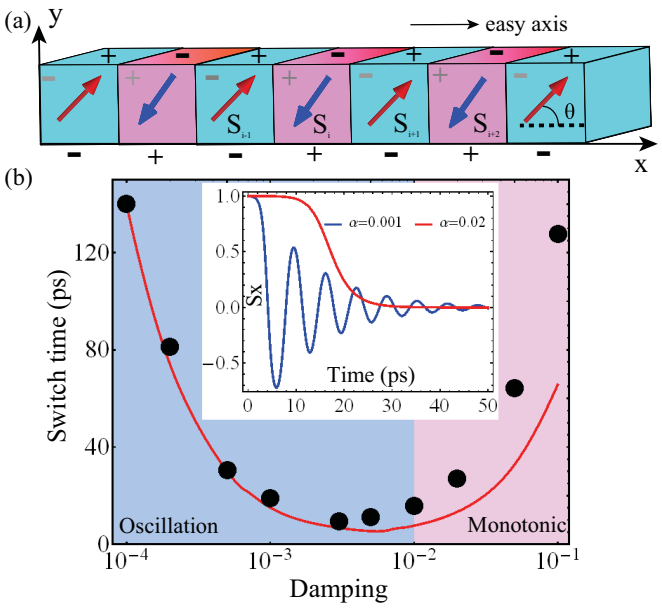

FIG. 1. (a) Schematic illustration of a two-sublattice antiferromagnetic nanowire. The red and blue arrows represent the magnetic moments on each sublattice. The easy axis of crystalline anisotropy is along the x axis. The plus and minus signs indicate the distribution of magnetic charges on the surface (black) and inside the volume (gray), respectively. (b) Switching time of magnetic order as a function of damping. The red line is the theoretical prediction of Eq. (6). The light blue and light pink regions represent the oscillating and monotonic phases, respectively. The inset shows the two typical switching modes in the two phases for $\alpha = 0.001$ (blue line) and $\alpha = 0.02$ (red line), respectively.

as shown in Fig. 1(a). The magnetization dynamics is first studied by numerically solving the Landau-Lifshitz-Gilbert (LLG) equation [21]

$$\frac{\partial \mathbf{S}_i}{\partial t} = -\gamma \mathbf{S}_i \times \mathbf{H}_i + \frac{\alpha}{S}\mathbf{S}_i \times \frac{\partial \mathbf{S}_i}{\partial t}, \tag{1}$$

where $\mathbf{S}_i$ is the dimensionless spin vector at the ith site with magnitude S, γ is the gyromagnetic ratio, and α is the Gilbert damping. In addition, $\mathbf{H}_i$ is the effective field acting on $\mathbf{S}_i$, including an antiferromagnetic exchange field between the two nearest spins, the crystalline anisotropy field, and the stray field. The effective field can be quantitatively evaluated as $\mathbf{H}_i = -\delta\mathcal{H}/\delta\mathbf{S}_i$. The Hamiltonian $\mathcal{H}$ reads

$$\mathcal{H} = J\sum_{\langle i,j\rangle} \mathbf{S}_i \cdot \mathbf{S}_j - K\sum_i \mathbf{S}_{i,x}^2 - \frac{\mu_0\mu_s}{2S}\sum_i \mathbf{S}_i \cdot \mathbf{H}_{d,i}, \tag{2}$$

where the first, second, and third terms represent the exchange, crystalline anisotropy, and magnetostatic energy, respectively. Further, J, K, μ_0, and μ_s are, respectively, the exchange coefficient, the crystalline anisotropy coefficient, the vacuum permeability, and the magnitude of local magnetic moments. In addition, $\mathbf{H}_{d,i}$ is the dipolar field acting on the spin $\mathbf{S}_i$. The factor $1/2$ is introduced to eliminate the duplicate calculation of magnetostatic energy.

To simulate the dynamics of the system, the parameters are taken to mimic the commonly used AFM Mn_2Au with $J = 24$ meV [22] and $\mu_s = 3.59\mu_B$, where μ_B is the Bohr magneton. Note that the anisotropy of Mn_2Au is sensitive to the magnitude of strain [23] and the magnitude of damping α is still lacking experimental characterization, and thus we treat them as free parameters. The following are our main findings. (i) The antiferromagnetic order switches spontaneously away from the easy axis (x axis) toward the transverse direction for crystalline anisotropy $K < 1.55$ μeV (15 mT). Two typical switching events are shown in the inset of Fig. 1(b). For $\alpha < \alpha_c \sim 0.01$, the switching is accompanied by ultrafast oscillation of magnetization, while the switching is monotonic for larger dampings. (ii) The switching time first decreases and then increases with the damping and the minimum is located around the critical damping, which separates the oscillation phase from the monotonic phase. In contrast, no switching happens for the ferromagnetic counterpart with exactly the same parameters except for the sign of the exchange coefficient J. Next we will show that this anomalous switching of an AFM resulting from the effect of MI and the oscillation/monotonic phase can be understood from the underdamped and overdamped phenomena of a pendulumlike motion of the AFM order parameter.

A. Theoretical formalism

To understand the anomalous switching behavior, the key point is to properly consider the demagnetization effect in this system. Here both the volume and surface charges contribute to the magnetostatic field $\mathbf{H}_d$, which can be formally evaluated as

$$\mathbf{H}_{d,i} = -M_s/S\sum_j \mathbf{N}_{ij}\cdot\mathbf{S}_j, \tag{3}$$

where $M_s = \mu_s/a^3$ is the saturation magnetization, with a the distance between two neighboring spins, and $\mathbf{N}_{ij}$ is the demagnetization tensor that depends only on the distance of two spins [24].

Suppose the system is in a Néel state with $\mathbf{S}_i = (-1)^i S(\cos\theta\mathbf{e}_x + \sin\theta\mathbf{e}_y)$, as shown in Fig. 1(a), and the longitudinal dimension $N \gg 1$; then the total energy of the system can be calculated as

$$E(\theta) = -(N-1)JS^2 - NKS^2\cos^2\theta + Na^3K_d(D_\parallel\cos^2\theta + D_\perp\sin^2\theta), \tag{4}$$

where $K_d = \mu_0 M_s^2/2$, $D_\parallel = N_{r=0}^{xx} + 2\sum_{p=1}^{N/2}(-1)^p N_{r=pa}^{xx}$, $D_\perp = N_{r=0}^{yy} + 2\sum_{p=1}^{N/2}(-1)^p N_{r=pa}^{yy}$, and $r = |i-j|a$ is the distance between two spins. The factor $(-1)^p$ comes from the antiparallel (parallel) alignment of two spins separated by an odd (even) distance a, which disappears for a ferromagnetic state. Since the magnetostatic energy of two spins decays with their distance as $1/r^3$ [25], two well-separated spins with large separation do not contribute to the energy significantly. Here we use a cutoff distance of $r = 4a$ and analytically derive $D_\parallel = 0.5713$ and $D_\perp = 0.2144$ by evaluating the demagnetization tensors N_r^{xx} and N_r^{yy} directly. A choice of a larger cutoff distance will not change $D_\parallel$ or $D_\perp$ more than 1%.

Here we pay special attention to the longitudinal magnetization states (LSs) $\theta = 0$ and transverse states (TSs) $\theta = \pi/2$. The energy difference of these two states can be explicitly

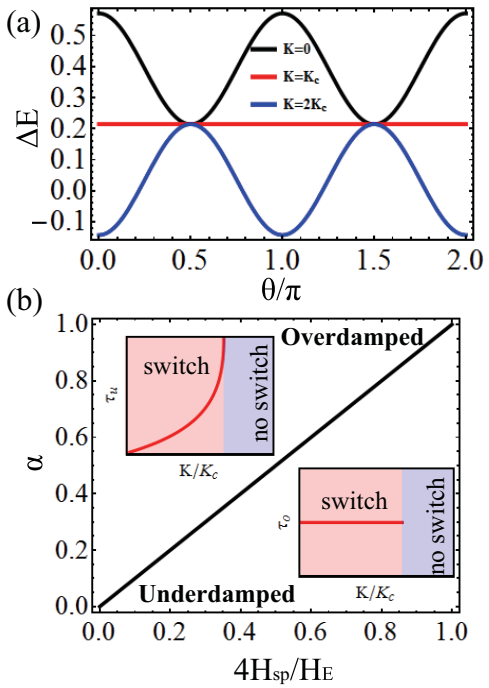

FIG. 2. Energy landscape of the system as a function of spin orientation θ for $K = 0$ (black line), $K = K_c$ (red line), and $K = 2K_c$ (blue line). The vertical axis is scaled by NK_d. (b) Phase diagram of the system in the $4H_{\rm sp}/H_E \sim \alpha$ plane. The top left and bottom right insets show the typical switching time as a function of crystalline anisotropy for the overdamped regime and the underdamped regime, respectively.

calculated as $\Delta E/N = -KS^2 + K_d(D_\parallel - D_\perp)$. For an AFM with strong crystalline anisotropy, the LS is energetically preferable while the TS becomes energetically preferable when the anisotropy is very weak. The critical anisotropy can be evaluated from $\Delta E = 0$ as $K_c = K_d(D_\parallel - D_\perp)$. Figure 2(a) shows the energy landscape of the system as a function of spin orientation θ for $K = 0$ (black line), $K = K_c$ (red line), and $K = 2K_c$ (blue line), respectively. Clearly, the LS (TS) has lower energy than the TS (LS) for $K > K_c$ ($K < K_c$). Then it is expected that the antiferromagnet will spontaneously switch from the LS to the TS for $K < K_c$, where the crystalline anisotropy can be reduced by electrical means [26–28].

To analytically describe this switching process, we recall the antiferromagnetic dynamic equations in terms of the staggered order [17]

$$\mathbf{n} \times (\partial_{tt}\mathbf{n} + \alpha H_E \partial_t \mathbf{n} - H_E \mathbf{h}_n) = 0, \tag{5}$$

where $\mathbf{n} \equiv (\mathbf{S}_{2i} - \mathbf{S}_{2i+1})/2S$ is the staggered order, $H_E \equiv 8JS$ is the homogeneous exchange field, and $\mathbf{h}_n = 4(K - K_c)\mathbf{e}_x$ is the effective anisotropy field acting on the staggered order. In spherical coordinates, the dynamic equations can be recast as

$$\frac{\partial^2 \psi}{\partial t^2} + 2\zeta\omega_0 \frac{\partial \psi}{\partial t} + \mathrm{sgn}(K - K_c)\omega_0^2 \sin\psi = 0, \tag{6}$$

where $\psi = 2\theta$, $\zeta = \alpha H_E/4H_{\rm sp}$, $\omega_0 = \gamma H_{\rm sp}$, $H_{\rm sp} = \sqrt{H_E K_{\rm eff}}$ is the spin-flop field, and $K_{\rm eff} = |K - K_c|$ is the effective anisotropy coefficient that includes the contribution from MI. The sign function $\mathrm{sgn}(x) = 1$ for $x \geqslant 0$ and -1 for $x < 0$. This equation is similar to the dynamics of a damped nonlinear pendulum [29]. In general, the solution to Eq. (6) is an elliptic function with a complicated time dependence [29]. To gain some insight into the timescale of the system, we will solve Eq. (6) using the small-amplitude approximation ($\sin\psi \sim \psi$).

According to the value of damping ratio ζ, three regimes can be classified. (i) For the underdamped regime $\zeta < 1$, i.e., $\alpha < 4H_{\rm sp}/H_E$, we have the solution $\psi(t) = \psi_0 e^{-\zeta\omega_0 t}\sin(\sqrt{1-\zeta^2}\omega_0 t + \varphi_0)$. The system oscillates and decays to the equilibrium state with a timescale of $\Delta t = 1/\zeta\omega_0$, i.e., the larger the damping is, the faster the relaxation will be. This is consistent with the oscillation phase in Fig. 2(b). (ii) For the overdamped regime $\zeta > 1$, i.e., $\alpha > 4H_{\rm sp}/H_E$, $\psi(t) = \psi_0 e^{-\zeta\omega_0 t}(c_1 e^{\sqrt{\zeta^2-1}\omega_0 t} + c_2 e^{-\sqrt{\zeta^2-1}\omega_0 t})$. Two modes $1/\tau_s = (\zeta - \sqrt{\zeta^2-1})\omega_0$ and $1/\tau_f = (\zeta + \sqrt{\zeta^2-1})\omega_0$ compete to determine the dynamics, while the long-time behavior of the pendulum is dominated by the slow mode τ_s. Since τ_s increases with the damping ratio, the relaxation time becomes larger with the increase of damping. This is also consistent with the monotonic phase in Fig. 2(b). (iii) For the critical regime $\zeta = 1$, i.e., $\alpha = 4H_{\rm sp}/H_E$, $\psi(t) = \psi_0 e^{-\zeta\omega_0 t}$. A complete phase diagram in the $4H_{\rm sp}/H_E \sim \alpha$ plane is shown in Fig. 2(b). The typical overdamped and underdamped cases are shown in the top left and bottom right insets, respectively. They show distinguished anisotropy dependences.

As a comparison, the ferromagnetic counterpart of Eq. (6) reads [30]

$$\frac{\partial \theta}{\partial t} = -\alpha\gamma K_{\rm eff}\sin 2\theta, \tag{7}$$

which is a first-order ordinary differential equation. This equation can be analytically solved as $-(t - t_0)/\Delta t = \ln\tan\theta$, where $\Delta t = 1/2\alpha\gamma K_{\rm eff}$. Differing from antiferromagnets, the typical switching time does not depend on the strong exchange constant H_E and it usually takes a longer time to reach the steady state because of $K_{\rm eff} \ll H_E$.

B. Two- and three-dimensional cases

Up until now, we have focused on the switching behavior of a one-dimensional (1D) magnetic nanowire, but the essential physics is still valid for the *C*-type antiferromagnet in the 2D and 3D cases. To be specific, as shown in Fig. 3(a), the magnetostatic field of a particular spin (dashed line) always aligns parallel (antiparallel) to the nearest spins for a TS (LS) in the *C*-type antiferromagnet. Hence, the TS is energetically favorable. For the *G*-type antiferromagnet or checkerboard antiferromagnet, the LS and TS are energetically degenerate, which can be seen in Fig. 3(b). For reference, Table I lists the strength of anisotropy coefficients induced by MI in various spin orderings of antiferromagnets, which is calculated using the technique presented in Sec. II A. As the spatial dimension increases from one dimension to three, the influence of the MI ($D_\parallel/D_\perp$) becomes more significant for *C*-type antiferromagnets.

Before going on, we emphasize that the effective anisotropy caused by MI is very different from the

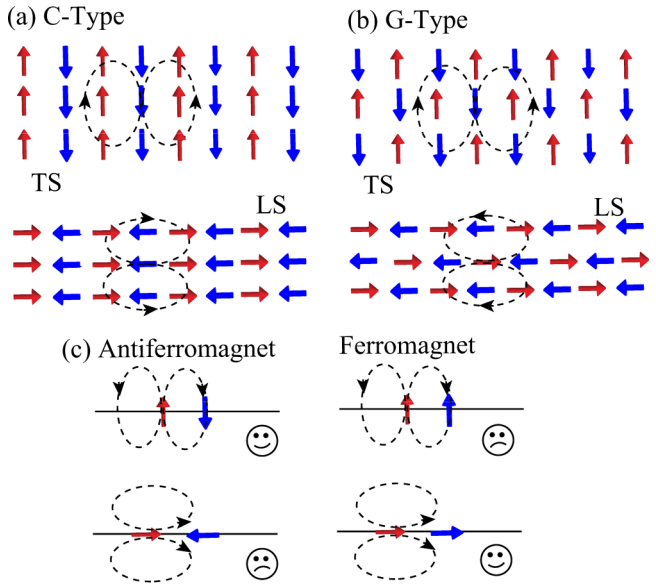

FIG. 3. Schematic illustration of an antiferromagnet with (a) C-type ordering and (b) G-type ordering in two dimensions. The dashed lines indicate the flow of magnetostatic fields generated by the central spin. (c) Schematic illustration of the difference between two antiferromagnetically and ferromagnetically coupled spins. The smiling and frowning faces refer to low-energy and high-energy states, respectively.

ferromagnetic counterpart known as the shape anisotropy. Use a 1D nanowire of sufficiently long length as an example, the demagnetization factor is $D_\parallel = 0$ and $D_\perp = 0.5$ for a ferromagnet,[1] which implies that the magnetization always tends to align in the longitudinal direction. For an antiferromagnet, the transverse direction is preferred by MI. This difference motivates this work, showing that the distribution of magnetic dipoles on an atomic scale will inevitably lead to a very different energy landscape of the system. A schematic illustration of this difference in a simple two-dipole model is given in Fig. 3(c); the physics is as follows. Along a line, the head-to-tail ferromagnetic state is the lowest energy state and the head-to-head antiferromagnetic configuration is the highest one. On the other hand, for two dipoles in a shoulder-to-shoulder configuration, the lower-energy configuration is the antiferromagnetic arrangement and the ferromagnetic one is the highest one.

C. Spin-wave spectrum modification

Theoretically, the spin-wave dispersion near an antiferromagnetic Néel state is [31,32]

$$\omega = \pm\gamma H + \gamma\sqrt{H_{\rm sp}^2 + 4J^2\sin^2 ka}, \tag{8}$$

where H is the external field and k is the spin-wave vector. For $k = 0$ and $H = 0$, we recover the magnetic resonance frequency $\omega_0 = \gamma\sqrt{H_{\rm E}K_{\rm eff}} = 2\gamma\sqrt{2JK_{\rm eff}}$. Since $K_{\rm eff} < K$ for $K > K_c$, the spin-flop field will become smaller under the influence of MI and the spin-wave frequency tends to have a redshift.

To verify these predictions, we add a magnetic field pulse $\mathbf{h}(t) = h_0\mathrm{sinc}(\omega t)\mathbf{e}_y$ to excite spin waves in an antiferromagnetic nanowire and calculate the time dependence of $\mathbf{S}(x,t)$ by numerically solving the LLG equation. By taking a 2D Fourier transform of $S_y(x,t)$, we obtain the spin-wave spectrum in the (k,ω) plane as shown in Figs. 4(a) ($K = 1.2K_c$), 4(b) ($K = 2K_c$), and 4(c) ($K = 10K_c$). Clearly, the dispersion can only be reproduced by including the influence of MI (white solid line), especially the magnetic resonance mode located at $k = 0$. As k increases, the influence of anisotropy becomes small, as indicated by the merging trend of the solid and dashed lines. We also plot the comparison of the resonance frequency as a function of crystalline anisotropy in Fig. 4(d). The role

TABLE I. List of the effective anisotropy coefficients generated by magnetostatic interaction in various spin orderings. Two-dimensional square lattices and 3D simple cubic lattices are used to calculated these values. The symbols CT and GT are short for C-type and G-type ordering, respectively.

Item	1D	2D CT	2D GT	3D CT	3D GT
$D_\parallel$	0.5713	0.7369	0.4163	0.9922	0.3350
$D_\perp$	0.2144	0.0022	0.4163	0.0028	0.3350

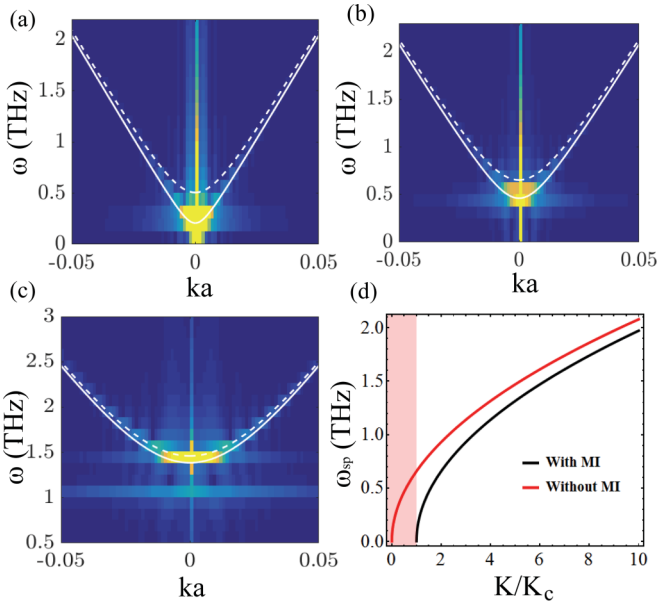

FIG. 4. Spin-wave spectrum of an antiferromagnetic nanowire after fully taking account of the magnetostatic interaction for (a) $K = 1.2K_c$, (b) $K = 2K_c$, and (c) $K = 10K_c$. The color codes the Fourier transform amplitude of $S_y(x,t)$. The white solid line is the theoretical prediction with MI while the white dashed line is the prediction without MI. (d) Magnetic resonance frequency as a function of crystalline anisotropy with MI (black line) and without MI (red line) for $H = 0$, $h_0 = 0.2$ T, $\omega = 10$ THz, and $\alpha = 10^{-4}$. The light red region indicates the regime in which spontaneous switching occurs.

[1]For a ferromagnet, we can follow a similar approach in Sec. II A and derive $D_\parallel = N_{r=0}^{xx} + 2\sum_{p=1}^{N/2} N_{r=pa}^{xx} \approx 0$ and $D_\perp = N_{r=0}^{yy} + 2\sum_{p=1}^{N/2} N_{r=pa}^{yy} \approx 0.5$.

of magnetostatic interaction becomes most significant when $K/K_c \to 1$.

III. ANTIFERROMAGNETIC RESONANCE

The magnetic resonance represents a large-amplitude oscillation of magnetic order when the driving frequency matches the natural frequency of the magnet. In experiments, by measuring the position of maximum absorption and the linewidth of the resonant spectrum, one can extract the magnetic parameters such as anisotropy and magnetic damping. In this section we show that this common understanding has some intrinsic problems for an antiferromagnet when the damping is close to a critical value, which is on the order of the ratio of the spin-flop field and the exchange field (~0.01 for $K_{\rm eff} \sim 10^{-4} H_{\rm E}$).

Let us start from the dynamic equations in terms of the two-sublattice magnetic moments [Eq. (1)]. Here we consider the regime $K > K_c$. By setting $\partial \mathbf{S}_i/\partial t = 0$, we find that the ground state of the system is a Néel state along the x axis, as shown in Fig. 1(a) with $\theta = 0$. Generally, the magnetic moments will perform uniform oscillations near this ground state under the action of an oscillating field $\mathbf{h} = \mathbf{h}e^{-i\omega t}$, i.e., $\mathbf{S}_{2i} = S\mathbf{e}_x + \delta\mathbf{S}_a(t)$ and $\mathbf{S}_{2i+1} = -S\mathbf{e}_x + \delta\mathbf{S}_b(t)$. By substituting the trial solutions into Eq. (1) and keeping only the terms linear in $\delta\mathbf{S}_{a,b}$, we obtain

$$i\frac{\partial}{\partial t}\begin{pmatrix}\delta S_a^+\\ \delta S_b^+\end{pmatrix} = \mathbf{D}\mathbf{H}_0\begin{pmatrix}\delta S_a^+\\ \delta S_b^+\end{pmatrix} + \mathbf{D}\begin{pmatrix}-h_+\\ h_+\end{pmatrix}, \tag{9}$$

where $\delta S_a^+ = \delta S_a^y + i\delta S_a^z$ and $h_+ = h_y + ih_z$. Here $\mathbf{D} = \mathrm{diag}((1-i\alpha)^{-1}, (1+i\alpha)^{-1})$ is the dissipation matrix and $\mathbf{H}_0$ is the effective Hamiltonian in the absence of damping,

$$\mathbf{H}_0 = \begin{pmatrix}-\Omega & -2JS\\ 2JS & \Omega\end{pmatrix}, \tag{10}$$

where $\Omega = 2JS + 2K_{\rm eff}$. Then the eigenspectrum can be determined by solving the secular equation $\det(\omega - D H_0) = 0$ as

$$\omega_r = \frac{1}{1+\alpha^2}\left[-i\alpha\gamma\Omega \pm \gamma\sqrt{H_{\rm sp}^2 - (\alpha H_E/4)^2}\right]. \tag{11}$$

One immediately sees that there exists a critical damping $\alpha_c = 4H_{\rm sp}/H_E$ above which the eigenfrequencies are purely imaginary, as shown in Fig. 5(a). Interestingly, this critical damping is exactly the boundary that separates the oscillation phase (underdamped regime) from the monotonic phase (overdamped regime) discussed in Sec. II A.

To see how the system responds to the electromagnetic wave, we can rewrite Eq. (9) by assuming $\delta S_{a,b}(t) = \delta S_{a,b} e^{-i\omega t}$,

$$\begin{pmatrix}\delta S_a^+\\ \delta S_b^+\end{pmatrix} = \begin{pmatrix}\chi_{aa} & \chi_{ab}\\ \chi_{ba} & \chi_{bb}\end{pmatrix}\begin{pmatrix}h_+\\ h_+\end{pmatrix}, \tag{12}$$

where

$$\chi_{aa} = \frac{\Omega - \omega - i\alpha\omega}{-\omega_0^2 + (1+\alpha^2)\omega^2 + 2i\alpha\Omega\omega},$$
$$\chi_{bb} = \frac{\Omega + \omega - i\alpha\omega}{-\omega_0^2 + (1+\alpha^2)\omega^2 + 2i\alpha\Omega\omega},$$

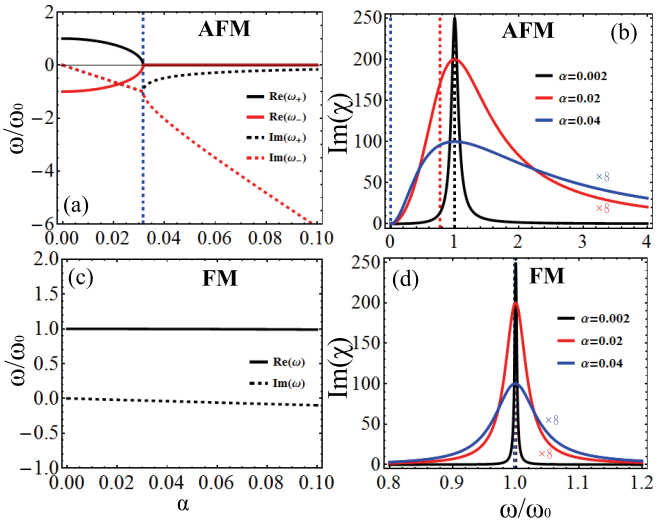

FIG. 5. (a) Eigenfrequencies as a function of damping. The blue dashed line denotes the position of critical damping α_c. (b) Absorption spectrum as a function of frequency for $\alpha = 0.002$ (black line), $\alpha = 0.02$ (red line), and $\alpha = 0.04$ (blue line). The dashed lines indicate the positions of the true resonance frequency ω_r at the corresponding damping. (c) and (d) Results for ferromagnets.

$$\chi_{ab} = \frac{-2JS}{-\omega_0^2 + (1+\alpha^2)\omega^2 + 2i\alpha\Omega\omega},$$
$$\chi_{ba} = \frac{-2JS}{-\omega_0^2 + (1+\alpha^2)\omega^2 + 2i\alpha\Omega\omega}. \tag{13}$$

Here we define the staggered order parameter as $\delta n = \delta S_a^+ - \delta S_b^+ = \chi_n h_+$; then χ_n can be calculated as

$$\chi_n = \frac{2\omega\left[\omega_0^2 - (1+\alpha^2)\omega^2 + 2i\alpha\Omega\omega\right]}{\left[\omega_0^2 - (1+\alpha^2)\omega^2\right]^2 + (2\alpha\Omega\omega)^2}. \tag{14}$$

The imaginary part of χ_n [$\mathrm{Im}(\chi_n)$] is related to the absorption of the system at microwave frequencies [33], which is maximal at $\omega_m = \omega_0/(1+\alpha^2)$.[2] When $\alpha = 0$, this peak position is coincident with the resonance frequency predicted by Eq. (11), i.e., $\omega_m = \omega_r$. Under a tiny damping, i.e., $\alpha \lll 1$, one can reduce χ_n to the widely used Lorentz form as

$$\mathrm{Im}(\chi_n) = \frac{\alpha\Omega}{(\omega - \omega_0)^2 + (\alpha\Omega)^2}. \tag{15}$$

Nevertheless, as damping further increases, we notice that the peak frequency of the line shape ω_m deviates from the real resonant frequency ω_r as

$$\frac{\omega_r}{\omega_m} = \sqrt{1 - \left(\frac{\alpha}{\alpha_c}\right)^2}. \tag{16}$$

For larger α, the deviation of ω_m with ω_r becomes larger and it gives a completely wrong prediction of ω_r when $\alpha \sim \alpha_c$, as shown in Fig. 5(b).

[2]One can analytically obtain ω_m by solving the equation $\partial\,\mathrm{Im}(\chi_n)/\partial\omega = 0$.

TABLE II. List of the critical damping in commonly used antiferromagnets. Note that the exchange fields have different definitions in these references; here we only estimate the order of α_c as $H_{\rm sp}/H_E$ for simplicity. There is no entry when no experimental values of dampings are found.

Material	Ref.	$H_E(T)$	$H_{\rm sp}(T)$	α_c	Expt. α
NiO	[34]	524	39	0.07	5×10^{-4}
MnO	[35]	127	29	0.23	<0.02
MnF_2	[36,37]	55.6	9.75	0.18	6×10^{-4}
α-Fe_2O_3	[38]	1040	6	0.006	
$LaMnO_3$	[39]	33.9	5.2	0.15	
Na_4^{3+} cluster	[40]	290	2.7	0.009	
MnTe	[41]	336	0.5	0.0015	
Mn_2Au	[42]	1300	5	0.004	
γ-MnCu	[43]	377	13	0.034	0.78

To resolve this anomaly, we first notice that the width of the line shape in Fig. 5(b) has become comparable to the resonance frequency when α is close to α_c. This suggests that the quality factor Q of the resonance is very small and thus the line shape is no longer reliable. To see this point clearly, we can solve the half-maximum width of the line shape $\Delta\omega = 4\alpha JS/(1+\alpha^2)$ by setting $\omega = \omega_m$ in Eq. (14) and derive the Q value as

$$Q = \frac{\omega_m}{\Delta\omega} = \frac{\alpha_c(1+\alpha^2)}{2\alpha} \approx \frac{\alpha_c}{2\alpha}. \tag{17}$$

At $\alpha = \alpha_c$, $Q = 1/2$ is very bad. This effect is intrinsic for all types of antiferromagnets, whether the quality of the sample is high or not. As a comparison, we can derive $Q = 1/2\alpha$ for a ferromagnet, which does not suffer from this problem as long as $\alpha \ll 1$, as shown in Figs. 5(c) and 5(d).

Physically, this difference between antiferromagnets and ferromagnets comes from their different dissipation mechanism. For an antiferromagnet, the magnetic moments on the two sublattices must tilt away from antiparallel orientations to launch the dissipation, while the antiferromagnetic exchange coupling H_E tends to suppress this tendency. As the exchange coupling becomes large, this channel will become highly inefficient, and therefore the resonant precession will be suppressed. For a ferromagnet, one magnetic moment simply dissipates through the Gilbert damping. The value of damping uniquely determines the speed of dissipation.

For reference, we summarize the typical values of critical dampings in Table II, which include antiferromagnetic insulators, semiconductors, and metals. They range from 10^{-3} to 10^{-1}. For most antiferromagnetic insulators, the intrinsic damping is expected to be smaller than 10^{-3}, from the experience of magnetic resonance. Hence they should be well below the critical damping and antiferromagnetic resonance is still a reliable technique to extract magnetic parameters. For antiferromagnetic metals, the situation becomes worse since the critical damping is considerably large compared with the real damping and the resulting line shape may deviate significantly from the Lorentz shape. This creates an intrinsic difficulty in analyzing the resonance signal and it is probably the reason why very few resonant experiments are available for antiferromagnetic metals.

IV. DISCUSSION AND CONCLUSION

Here we would like to comment on the conventional wisdom of the AFM community. It was taken for granted that MI in AFMs is negligible without any proof. Thus MI is neglected in most, if not all, of the analytical models, numerical simulations, and the analysis of AFM experimental results. Hence it is not surprising that results found here were not predicted early. Of course, MI naturally exists in experiments, and one should be very careful to explain the experimental data by the theory without MI effects, especially when extracting the anisotropy coefficients.

In conclusion, we have studied MI effects on the antiferromagnetic dynamics. Even though the total magnetic charges of an AFM as well as the resulting magnetostatic field outside the system are vanishingly small, the local charge distribution at the atomic scale could considerably modify the system anisotropy in magnetic nanowires as well in quasi-2D and -3D structures. By analytically evaluating the effective dipolar anisotropy, we find that MI could even change the easy axis of a properly designed nanostructure. We found that the switching time first decreases and then increases with the damping. The underdamped and overdamped phases are thus classified, resembling the motion of a nonlinear pendulum. Near the phase boundary, the line shape of the AFM resonance becomes non-Lorentzian with a very low quality factor and thus it is no longer reliable to extract the magnetic parameters in this case.

ACKNOWLEDGMENTS

H.Y.Y. acknowledge Jiang Xiao for helpful discussions. The work was financially supported by National Natural Science Foundation of China (NSFC) under Grant No. 61704071 and Shenzhen Fundamental Subject Research Program under Grant No. JCYJ20180302174248595. M.-H.Y. acknowledges support from the Guangdong Innovative and Entrepreneurial Research Team Program (Grant No. 2016ZT06D348) and Science, Technology and Innovation Commission of Shenzhen Municipality (Grants No. ZDSYS20170303165926217 and No. JCYJ20170412152620376). X.R.W. was supported by the NSFC (Grant No. 11774296) and Hong Kong RGC (Grants No. 16301518, No. 16301619, and No. 16300117).

[1] P. Wadley *et al.*, Science **351**, 587 (2016).
[2] J. Železný, H. Gao, K. Výborný, J. Zemen, J. Mašek, A. Manchon, J. Wunderlich, J. Sinova, and T. Jungwirth, Phys. Rev. Lett. **113**, 157201 (2014).
[3] Q. Liu, H. Y. Yuan, K. Xia, and Z. Yuan, Phys. Rev. Materials **1**, 061401(R) (2017).
[4] H. Y. Yuan, Q. Liu, K. Xia, Z. Yuan, and X. R. Wang, Europhys. Lett. **126**, 67006 (2019).

[5] A. V. Kimel, A. Kirilyuk, A. Tsvetkov, R. V. Pisarev, and T. Rasing, Nature (London) **429**, 850 (2004).
[6] R. A. Duine, P. M. Haney, A. S. Nunez, and A. H. MacDonald, Phys. Rev. B **75**, 014433 (2007).
[7] P. M. Haney and A. H. MacDonald, Phys. Rev. Lett. **100**, 196801 (2008).
[8] Y. Xu, S. Wang, and K. Xia, Phys. Rev. Lett. **100**, 226602 (2008).
[9] R. Cheng, J. Xiao, Q. Niu, and A. Brataas, Phys. Rev. Lett. **113**, 057601 (2014).
[10] K. M. D. Hals, Y. Tserkovnyak, and A. Brataas, Phys. Rev. Lett. **106**, 107206 (2011).
[11] O. Gomonay, T. Jungwirth, and J. Sinova, Phys. Rev. Lett. **117**, 017202 (2016).
[12] T. Shiino, S. H. Oh, P. M. Haney, S.-W. Lee, G. Go, B.-G. Park, and K.-J. Lee, Phys. Rev. Lett. **117**, 087203 (2016).
[13] S. Selzer, U. Atxitia, U. Ritzmann, D. Hinzke, and U. Nowak, Phys. Rev. Lett. **117**, 107201 (2016).
[14] T. Jungwirth, X. Marti, P. Wadley, and J. Wunderlich, Nat. Nanotech. **11**, 231 (2016).
[15] X. Zhang, Y. Zhou, and M. Ezawa, Sci. Rep. **6**, 24795 (2016).
[16] J. Barker and O. A. Tretiakov, Phys. Rev. Lett. **116**, 147203 (2016).
[17] H. Y. Yuan, W. Wang, M.-H. Yung, and X. R. Wang, Phys. Rev. B **97**, 214434 (2018).
[18] H. Y. Yuan, M.-H. Yung, and X. R. Wang, Phys. Rev. B **98**, 060407(R) (2018).
[19] H. V. Gomonay and V. M. Loktev, Phys. Rev. B **81**, 144427 (2010).
[20] M. J. Stephen and J. P. Straley, Red. Mod. Phys. **46**, 617 (1974).
[21] A. Vansteenkiste, J. Leliaert, M. Dvornik, M. Helsen, F. Garcia-Sanchez, and B. Van Waeyenberge, AIP Adv. **4**, 107133 (2014).
[22] A. A. Sapozhnik, C. Luo, H. Ryll, F. Radu, M. Jourdan, H. Zabel, and H.-J. Elmers, Phys. Rev. B **97**, 184416 (2018).
[23] A. B. Shick, S. Khmelevskyi, O. N. Mryasov, J. Wunderlich, and T. Jungwirth, Phys. Rev. B **81**, 212409 (2010).
[24] A. J. Newell, W. Williams, and D. J. Dunlop, J. Geophys. Res. **98**, 9551 (1993).
[25] J. D. Jackson, *Classical Electrodynamics*, 3rd ed. (Wiley, New York, 1998).
[26] M. Weisheit, S. Fähler, A. Marty, Y. Souche, C. Poinsignon, and D. Givord, Science **315**, 349 (2007).
[27] T. Maruyama, Y. Shiota, T. Nozaki, K. Ohta, N. Toda, M. Mizuguchi, A. A. Tulapurkar, T. Shinjo, M. Shiraishi, S. Mizukami, Y. Ando, and Y. Suzuki, Nat. Nanotech. **4**, 158 (2009).
[28] D. Lebeugle, A. Mougin, M. Viret, D. Colson, and L. Ranno, Phys. Rev. Lett. **103**, 257601 (2009).
[29] K. Johannessen, Eur. J. Phys. **35**, 035014 (2014).
[30] Y. Zhang, H. Y. Yuan, X. S. Wang, and X. R. Wang, Phys. Rev. B **97**, 144416 (2018).
[31] W. Wang, C. Gu, Y. Zhou, and H. Fangohr, Phys. Rev. B **96**, 024430 (2017).
[32] H. Y. Yuan and X. R. Wang, Appl. Phys. Lett. **110**, 082403 (2017).
[33] Y. Zhang, X. S. Wang, H. Y. Yuan, S. S. Kang, H. W. Zhang, and X. R. Wang, J. Phys.: Condens. Matter **29**, 095806 (2017).
[34] T. Moriyama, K. Hayashi, K. Yamada, M. Shima, Y. Ohya, and T. Ono, Phys. Rev. Materials **3**, 051402(R) (2019).
[35] A. J. Sievers and M. Tinkham, Phys. Rev. **129**, 1566 (1963).
[36] F. M. Johnson and A. H. Nethercot, Phys. Rev. **114**, 705 (1959).
[37] J. P. Kotthaus and V. Jaccarino, Phys. Rev. Lett. **28**, 1649 (1972).
[38] R. Lebrun, A. Ross, O. Gomonay, S. A. Bender, L. Baldrati, F. Kronast, A. Qaiumzadeh, J. Sinova, A. Brataas, R. A. Duine, and M. Klaui, Commun. Phys. **2**, 50 (2019).
[39] D. Talbayev, L. Mihaly, and J. Zhou, Phys. Rev. Lett. **93**, 017202 (2004).
[40] T. Nakano, H. Tsugeno, A. Hanazawa, T. Kashiwagi, Y. Nozue, and M. Hagiwara, Phys. Rev. B **88**, 174401 (2013).
[41] D. Kriegner *et al.*, Phys. Rev. B **96**, 214418 (2017). Here we estimate the exchange field from the Néel temperature of MnTe.
[42] V. M. T. S. Barthem, C. V. Colin, H. Mayaffre, M.-H. Julien, and D. Givord, Nat. Commun. **4**, 2892 (2013).
[43] M. C. K. Wiltshire and M. M. Elcombe, Physica B+C **120**, 167 (1983).